Li *et al. Energy Mater* 2023;3:300021
DOI: 10.20517/energymater.2023.09

Energy Materials

Article

Open Access

Check for updates

Iron phthalocyanine coupled with nickel-iron selenide layered hydroxide derivative as dual-functional oxygen electrocatalyst for rechargeable zinc-air batteries

Guang Li[1], Kuang Sheng[2], Yu Lei[1], Feng Zhang[1], Juan Yang[1], Baobao Chang[3], Liping Zheng[1,*], Xianyou Wang[1,*]

[1]National Base for International Science & Technology Cooperation, National Local Joint Engineering Laboratory for Key Materials of New Energy Storage Battery, Hunan Province Key Laboratory of Electrochemical Energy Storage & Conversion, School of Chemistry, Xiangtan University, Xiangtan 411105, Hunan, China.
[2]School of Chemistry and Chemical Engineering, Central South University, Changsha 410083, Hunan, China.
[3]Key laboratory of Materials Processing and Mold of Ministry of Education, Zhengzhou University, Zhengzhou 450001, Henan, China.

[*]**Correspondence to:** Liping Zheng, National Base for International Science & Technology Cooperation, National Local Joint Engineering Laboratory for Key Materials of New Energy Storage Battery, Hunan Province Key Laboratory of Electrochemical Energy Storage & Conversion, School of Chemistry, Xiangtan University, North Second Ring Road, Yuhu District, Xiangtan 411105, Hunan, China. E-mail: zlp33520@163.com; Prof. Xianyou Wang, National Base for International Science & Technology Cooperation, National Local Joint Engineering Laboratory for Key Materials of New Energy Storage Battery, Hunan Province Key Laboratory of Electrochemical Energy Storage & Conversion, School of Chemistry, Xiangtan University, North Second Ring Road, Yuhu District, Xiangtan 411105, Hunan, China. E-mail: xywang@xtu.edu.cn

How to cite this article: Li G, Sheng K, Lei Y, Zhang F, Yang J, Chang B, Zheng L, Wang X. Iron phthalocyanine coupled with nickel-iron selenide layered hydroxide derivative as dual-functional oxygen electrocatalyst for rechargeable zinc-air batteries. *Energy Mater* 2023;3:300021. https://dx.doi.org/10.20517/energymater.2023.09

Received: 12 Feb 2023 **First Decision:** 7 Mar 2023 **Revised:** 22 Mar 2023 **Accepted:** 30 Mar 2023 **Published:** 8 May 2023

Academic Editors: Hao Liu, Jiazhao Wang **Copy Editor:** Fangling Lan **Production Editor:** Fangling Lan

Abstract

The oxygen reduction reaction (ORR) and oxygen evolution reaction (OER) for dual-functional non-precious metal electrocatalysts are promising alternatives for Pt/Ru-based materials in rechargeable zinc-air batteries (ZABs). However, how to achieve dual-functional oxygen electrocatalytic activity on single-component catalysts and identify the sites responsible for ORR and OER still face many challenges. Herein, an efficient and stable dual-functional electrocatalyst is fabricated by a two-step hydrothermal method with iron phthalocyanine (FePc) π-π stacking on nickel-iron selenide layered hydroxide derivatives ($Se/Ni_3Se_4/Fe_3O_4$). The as-prepared multi-component catalyst (named as FePc/Se@NiFe) exhibits better oxygen electrocatalytic properties than Pt/Ru-

based catalysts, with a half-wave potential ($E_{1/2}$) of 0.90 V and an overpotential of 10 mA cm^{-2} (E_{j10}) of 320 mV. More importantly, chronoamperometry (I-T) and accelerated durability tests (ADT) show the unordinary stability of the catalyst. Both physical characterization and experimental results verify that the Fe-N_4 moieties and Ni_3Se_4 crystalline phase are the main active sites for ORR and OER activities, respectively. The small potential gap ($\Delta E = E_{j10} - E_{1/2}$ = 0.622 V) represents superior dual-functional activities of the FePc/Se@NiFe catalyst. Subsequently, the ZABs assembled using FePc/Se@NiFe exhibit excellent performances. This study offers a promising design concept for promoting further development of high-performance ORR and OER electrocatalysts and their application in ZAB.

Keywords: Multi-component, layered double hydroxide, iron (II) phthalocyanine, dual-functional electrocatalyst, rechargeable zinc-air battery

INTRODUCTION

The critical energy security and environmental degradation issues caused by the depletion of traditional fossil fuels have prompted a renewed focus on energy harvesting from renewable sources[1,2]. Rechargeable ZABs are considered to be one of the most promising energy storage and conversion devices because of their high specific capacity (≈820 mAh g^{-1} based on Zn metal), inherent safety, economical cost, and zero pollution[3-6]. The development of reliable dual-functional air electrode catalysts is one of the major challenges for ZABs, as it is the key to guarantee high conversion efficiency and long cycle life of batteries. Specifically, the charge-transfer kinetics of the ORR and OER at the air electrode are intrinsically sluggish during the discharge and charge processes[7]. Pt/C and IrO_2 (or RuO_2) are traditionally used as standard ORR and OER electrocatalysts, while dual-functional activity is achieved by their simple mixing. However, owning the inherent drawbacks such as particularly poor bifunctional oxygen activity, high prices, and earth scarcity, these precious metal-based catalysts hinder their long-term industrial application for rechargeable ZABs. To address these issues, great efforts have been made to develop dual-functional oxygen electrocatalysts without precious metals as alternatives[8].

In recent decades, 3d transition metal-based compounds characterized by earth-abundant resources and low cost have been developed as noble-metal-free catalysts, including transition metal-based sulfides[9,10], phosphides[11,12], carbides[13,14], and alloys[15], layer double hydroxides (LDHs)[16,17], and selenides[18,19]. Among them, the LDHs catalysts, especially NiFe-LDHs, have received much attention because of their prominent OER catalytic activity in alkaline solutions[20]. Generally, NiFe-LDHs have a special two-dimensional flake crystal structure of brucite, in which the solvent molecules and anionic groups are located between the layers of metal cations[21]. Because of the unique layered structure of NiFe-LDH, the performance of NiFe-LDH can be improved in a wide range by adjusting the types of anions and solvent molecules between wide layer spacing. This makes NiFe-LDHs considered to be a suitable material for OER catalytic process[22]. Although LDH-based catalysts exhibit relatively impressive OER performance, the self-agglomeration of nanoparticles and insufficient exposure of active sites are important factors limiting the further improvement of OER intrinsic activity[23]. Therefore, in order to improve the catalytic properties of NiFe-LDH to OER, a variety of strategies have been proposed, such as defect engineering[24], interface engineering[25,26], heteroatom doping[27,28], crystalline phase engineering[29,30], and morphology control[31,32]. Among these strategies, constructing a polycrystalline phase composite catalyst by crystalline phase engineering is a useful pathway to achieve high-performance OER electrocatalytic activities. Each phase in the polycrystalline phase is considered as the real catalytic active site. For example, Hong *et al.* reported a new and simple strategy, "dual-phase engineering", in which phase catalysts based on efficient transition metal hydroxides and high metal transition metal boride phases are used in OER[33]. Lou group synthesized two-component $Co_3O_4/NiCo_2O_4$ nanocages with OER activity beyond that of single-component Co_3O_4 or

$NiCo_2O_4$ nanocrystals[34]. Compared with borides and oxides, transition metal selenide nanocrystals, which have been reported, can potentially enhance further the OER catalytic performance because of their high density of active sites and excellent intrinsic catalytic activities. Especially, nickel selenide nanocrystals with unique electron vacancies and special hybrid orbitals possess expectantly activity in OER electrocatalysis[35]. Also, the formation of nickel hydroxide or selenium oxide plays an important role in the OER process. Zheng *et al.* synthesized a series of Ni_xSe ($0.5 \leq x \leq 1$) nanocrystals with different compositions as potential OER electrocatalysts[36]. The analysis reveals that $Ni_{0.5}Se$ nanocrystalline exhibits better OER catalytic activity than counterparts and noble metals. Up to now, although many multiphase selenide nanocrystals with excellent properties have been explored, the understanding of determining phase-dependent properties is still limited. In addition, the ORR performances are relatively unsatisfactory. To address ORR activity issue, one promising approach is incorporating composite with splendid ORR materials with high intrinsic activity, such as Co/NC[37], Co porphyrin[38], $FeNi_3$/NC[39], FeSo-yCNSs-A[40], Fe_{SA}-N-C[41], and so on. For these catalysts, transition metal-N_X species is a key factor for obtaining high ORR activity. More importantly, atomically dispersed Fe-N_X species are considered to be the most active platinum group metal-free ORR catalysts. Transition metal phthalocyanines, as typical M-N_X ($x = 2, 4$) moieties, have been widely investigated due to their presented exceptional ORR activities. Among different phthalocyanine catalysts based on 3d transition metals (Co, Ni, Cu, and Mn), FePc-based catalysts with Fe-N_4 as the characteristic structure exhibited the best catalytic activity[42].

In this work, we report a FePc π-π conjugation interaction on Se@NiFe composites (FePc/Se@NiFe) via a facile hydrothermal procedure for the purpose of improving the ORR/OER activities and ZAB performance. As verified by physical characterization evidence, the dual-functional catalyst is composed of Fe-N_4 species and Se, Fe_3O_4, and Ni_3Se_4 crystal phases. In addition, we found that the FePc not only provides a carbon source to increase the conductivity of the catalyst, but also introduces defects to modify the electronic structure of the catalyst. Combining the electrochemical measurements results, the metallic Fe-N_4 ligand species are responsible for ORR, while Ni_3Se_4 crystal phases are the best OER active sites. The resultant FePc/Se@NiFe material shows remarkable dual-functional oxygen catalytic activity and ZABs performance indicators, outperforming that of benchmark Pt/C + RuO_2 in alkaline media. These results suggest that the FePc/Se@NiFe may be a potential candidate for practical energy technologies in alkaline medium, and it also helps to understand the precise ORR and OER active sites.

EXPERIMENTAL

Chemicals and reagents

Nickel(II) nitrate hexahydrate ($Ni(NO_3)_2 \cdot 6H_2O$, ≥ 99%), iron(III) nitrate nonahydrate [$Fe(NO_3)_3 \cdot 9H_2O$, ≥ 99%], ammonium fluoride (NH_4F, 99.99%), urea [$CO(NH_2)_2$, AR], iron phthalocyanine (FePc, 98%), and ruthenium(IV) oxide (RuO_2, 99.9%) were purchased from Macklin Reagent Biochemical Co., Ltd (Shanghai, China). Ethanol absolute (C_2H_5OH, 99.9%) and hydrazinehydrate diamidhydrate ($N_2H_4 \cdot H_2O$, 36%~38%) were obtained from Sinopharm Chemical Reagent Co., Ltd. Nafion (5%) and Pt/C (20%) were distributed from DuPont and Johnson Matthey companies (USA). ultrapure water (18 MΩ·cm^{-1}) was produced from Millipore system for all experiments. All the above chemical reagents were directly used.

Materials synthesis

Synthesis of the NiFe-LDH, Ni-LDH, and Fe-LDH precursor: NiFe-LDH was prepared by hydrothermal reaction. Specifically, $Ni(NO_3)_2 \cdot 6H_2O$ (0.67 mmol), $Fe(NO_3)_3 \cdot 9H_2O$ (0.33 mmol), NH_4F (4.0 mmol), and urea (6.0 mmol) were separately dissolved in 60 mL of deionized water (18.2 MΩ·cm). The solution was stirred vigorously for 30 min to obtain a light blue solution, and then transferred to an autoclave lined with 100 mL Teflon and subjected to hydrothermal reaction at 120 °C for 12 h. Subsequently, the precursor was gained by filtration and washing with deionized water and dried under vacuum at 60 °C. Finally, the yellow powder

was obtained and named NiFe-LDH. Ni-LDH and Fe-LDH were prepared in the same way as NiFe-LDH, except that $Fe(NO_3)_3 \cdot 9H_2O$ and $Ni(NO_3)_2 \cdot 6H_2O$ were not added, respectively.

Synthesis of the Se@NiFe: First, 79 mg of NiFe-LDH was dispersed in 57 mL of deionized water with the aid of ultrasonication (labeled as A solution). 79 mg of selenium powder was dispersed into 3 mL of hydrazine hydrate solution (labeled as B solution). Then, A and B solutions were mixed and stirred for 4 h. Finally, the above mixed solution was reacted in a 100 mL Teflon-lined autoclave at 100 °C for 6 h. The product Se@NiFe was achieved after washing with deionized water and vacuum drying at 60 °C.

Synthesis of the FePc/Se@NiFe: The synthesis process for FePc/Se@NiFe was the same as the above-mentioned one. Specifically, 10 mg of FePc was dispersed into 10 mL of absolute ethanol and ultrasonically treated for 30 min (labeled as A solution); 79 mg of selenium powder was dispersed into 3 mL of hydrazine hydrate solution (labeled as B solution); 79 mg of NiFe-LDH was ultrasonically dispersed in 47 mL of deionized water (labeled as C solution). Next, the three solutions of A, B and C were stirred for another 4 h. The resulting mixture was then poured into a 100 mL Teflon-lined autoclave and reacted at 100 °C for 6 h. The final FePc/Se@NiFe was obtained by washing with deionized water and drying under vacuum at 60 °C. The synthesis of FePc/Se@Ni was by converting the NiFe-LDH precursor to Ni-LDH and FePc/Se@Fe uses Fe-LDH as the precursor.

Material characterizations

X-ray powder diffraction (XRD) was performed on a Bruker D8 Advance diffractometer with Cu Kα radiation (λ = 0.154178 nm) at room temperature. The X-ray photoelectron spectroscopy (K-Alpha 1063) was employed to detect the element compositions and valence states of catalysts, and all the peaks were corrected by the standard of C 1s line at 284.8 eV. The carbon defects and graphitization degree were measured by Raman spectroscopy (InVia). The specific surface area (SSA) and pore volume of samples were tested with N_2 adsorption and desorption isotherms by Brunauer-Emmett-Teller (BET) (Micromeritics ASAP 2020). The structural morphologies of catalysts were observed by employing a high-resolution transmission electron microscope (HRTEM, FEI Tecnai F20) and field-emission scanning electron microscope (FESEM, Zeiss sigma 300). The relevant elemental distributions were presented by using energy-dispersive X-ray spectroscopy (EDX).

Electrochemical measurements

The electrochemical performance of the prepared catalyst was tested on CHI660E by a traditional three-electrode system. The electrolyte solution was 0.1 M KOH (ORR) or 1.0 M KOH (OER), Ag/AgCl (saturated KCl solution) was used as a reference electrode, and a platinum sheet was used as an auxiliary electrode. The ORR test was a glassy carbon electrode with a catalyst mass loading of 0.75 mg cm^{-2} and the OER test was a carbon paper electrode loaded with 0.75 mg cm^{-2} catalyst. All cyclic voltammetry (CV) tests were operated at a scan rate of 50 $mV \cdot s^{-1}$, and linear sweep voltammetry (LSV) tests were executed at a scan rate of 5 $mV \cdot s^{-1}$. Double-layer capacitance (C_{dl}) data were acquired by CV at different scan rates of 2, 4, 6, 8, and 10 $mV \cdot s^{-1}$ in the absence of faradaic current. Tafel slope was determined by the following equation: $\eta = b \log(j) + a$, where η, b and j are the overpotential, Tafel slope, the current density, respectively. The electrochemically active surface area (ECSA) could be calculated by $ECSA = S \times C_{dl}/C_s$ equation, where C_s values were 0.04 mF/cm^2 in alkaline conditions. Accelerated durability test (ADT) was conducted between -0.3~-0.8 V and 0.2~0.7 V at 100 mV s^{-1} in 0.1 M KOH (O_2-saturated) and 1.0 M KOH electrolytes (O_2-saturated), and then measured the LSV curve. The relative current of the I-T curve was also a means of assessing stability. The electron transfer number (n) of catalysts was figured below in the following Koutechy-Levich (K-L) equation:

$$\frac{1}{J} = \frac{1}{J_L} + \frac{1}{J_K} = \frac{1}{B\omega^{1/2}} + \frac{1}{J_K} \quad (1)$$

$$B = 0.62nF(D_0)^{2/3}(\nu)^{-1/6}C_0 \quad (2)$$

where the constants related to O_2 were different in alkaline (C_0 = 1.2 × 10^{-6} mol cm^{-1}; D_0 = 1.9 × 10^{-5} cm^2 s^{-1}) conditions. Other constants were fixed, which can refer to our previous work[43]. All potentials used in this effort were converted to potentials with respect to the reversible hydrogen electrode (RHE) by using the Nernst equation:

$$E_{RHE} = E_{Hg/Hg_2Cl_2} + 0.241 + 0.059 \times pH \quad (3)$$

The n and H_2O_2 yield were calculated by the rotating ring disk electrode (RRDE) tests with the following equation:

$$n = 4 \times \frac{I_d}{I_d + I_r/N_c} \quad (4)$$

$$H_2O_2\ \% = 200\frac{\frac{I_r}{N_c}}{I_d + \frac{I_r}{N_c}}\% \quad (5)$$

where I_d, I_r and N_c are all fixed value constants.

Assembly of rechargeable ZABs

Measurements of rechargeable liquid ZABs with our catalyst were accomplished using home-built electrochemical cells under atmosphere condition. Polished zinc plates were used as anode, and carbon cloth coated with homemade or Pt/C (J-M 20%) catalyst mass of 0.75 mg cm^{-2} was served as air cathode. The mixture solution of 6.0 M KOH + 0.2 M zinc acetate was used as alkaline electrolyte. The LSV charging/discharging curves were collected by CHI660E electrochemical workstation, and all other performance tests were performed using a Neware battery test system.

RESULTS AND DISCUSSION

Synthesis and structural investigations of the electrocatalyst

As illustrated in Scheme 1, the FePc/Se@NiFe sample was synthesized via a two-step hydrothermal process. Firstly, through a simple hydrothermal method, the NiFe-LDH nanosheet precursor was fabricated in a mixed solution of Ni^{2+} and Fe^{3+} salts. A detailed procedure was shown in the Experimental Section. Then, the collected NiFe-LDH nanosheet experienced an adequate wet chemical selenization during the secondary hydrothermal process in the environment of selenium and FePc solution at 100 °C. As the interlayer hydroxyl or carbanion anion of NiFe-LDH was replaced by Se^{2-} during this process, the derived polycrystals were supported by FePc nanoclusters. The crystalline phase and structure of the FePc, NiFe-LDH, Se@NiFe, FePc/Se@NiFe, FePc/Se@Ni and FePc/Se@Fe materials were analyzed by XRD analysis. As shown in Figure 1A, the pattern of FePc/Se@NiFe with peaks located at 30.1°, 35.4°, 56.9°, and 62.5° could be ascribed to the (220), (311), (511), and (440) crystal planes of Fe_3O_4, separately (PDF #19-0629)[44]. Peaks at 33.3°, 33.6°, 45.1°, 45.4°, and 50.8° are the (-312), (-402), (-514), (-604), and (-310) characteristic crystalline planes belonging to Ni_3Se_4 (PDF #89-2020)[45], while the peak at 23.5°, 29.7°, and 43.6° can match very well with the (110), (101), and (012) lattice planes of the Se (PDF #86-2246)[46], respectively. The above XRD

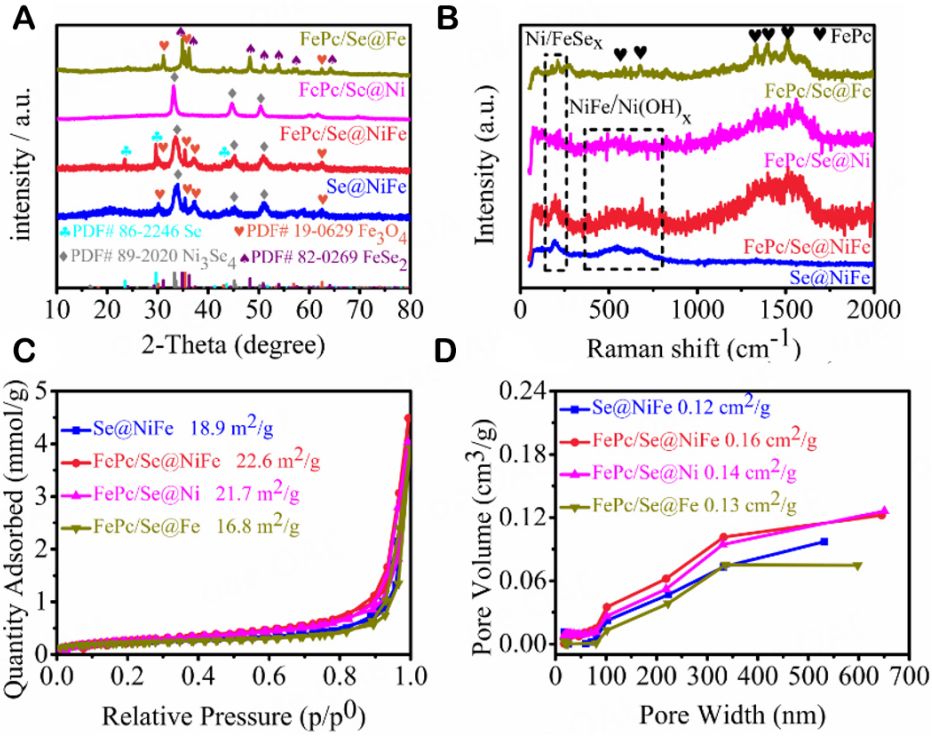

Figure 1. (A) XRD patterns, (B) Raman Spectroscopies, (C) Nitrogen adsorption and desorption isotherms, and (D) Pore volume of Se@NiFe, FePc/Se@NiFe, FePc/Se@Ni, and FePc/Se@Fe.

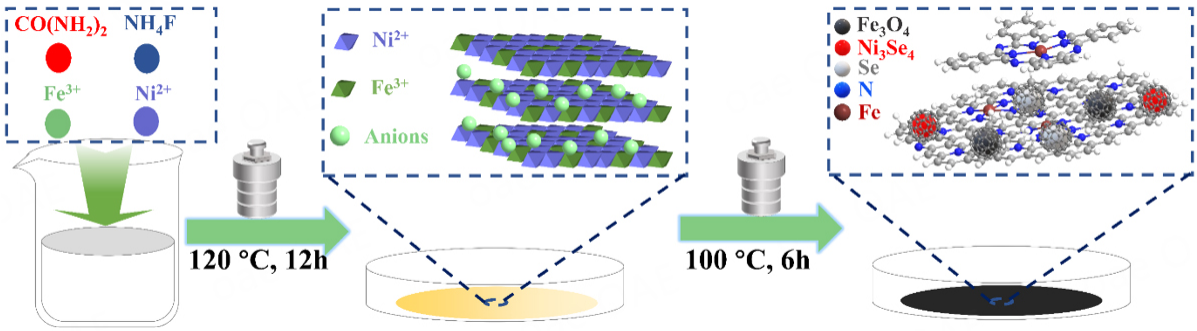

Scheme 1. Schematic illustration of the preparation processing of FePc/Se@NiFe.

patterns confirm the successful fabrication of Fe_3O_4, Se, and Ni_3Se_4 tri-phase nanocrystals hybrids. Equally, the same weak peaks in the XRD spectrum of Se@NiFe could also be observed, meaning that its crystalline structure will not be destroyed by a small amount of FePc dopant. As contrast samples, FePc/Se@Ni and FePc/Se@Fe were synthesized via a similar procedure to FePc/Se@NiFe (see Experimental Section). The characteristics of the XRD patterns indicated that FePc/Se@Ni forms a Ni_3Se_4 single phase, while FePc/Se@Fe forms a $FeSe_2$ and Fe_3O_4 dual phase. The above results indicate that Ni_3Se_4 is the active crystal phase that contributes the most to the OER process. It should be noted that there was no characteristic peak of FePc in the XRD patterns of all FePc mixed selenides, which is due to the small content of FePc in these electrocatalysts. The XRD patterns of FePc and NiFe-LDH precursors were provided in support information [Supplementary Figure 1A]. The diffraction peaks of the NiFe-LDH are in good agreement with the standard cards (PDF #26-1286)[47], indicating that pure NiFe-LDH was formed. In order to further

investigate the structural properties of the prepared samples, Raman spectroscopy was performed on them. As depicted in Supplementary Figure 1B, NiFe-LDH exhibits two distinct peaks at 462 and 542 cm^{-1}, which is consistent with previously reported results in the literature[48]. The low-intensity peak of FePc component at FePc/Se@NiFe and FePc/Se@Ni in the Raman spectrum confirms better dispersity [Figure 1B]. And the obvious high intensity Raman peak of FePc/Se@Fe is similar to that of FePc, demonstrating that FePc molecules mainly aggregate on the surface of Se@Fe[49]. Obviously, FePc/Se@NiFe and FePc/Se@Ni display a low-intensity characteristic peak of FePc that can indicate that Se@NiFe or Se@Ni may be connected with FePc by π-π conjugation interaction[42]. The above results can also be attributed to the fact that NiFe-LDH and Ni-LDH have a laminar structure that can adsorb and accommodate part of the FePc, which in turn helps to promote π-π interaction. In addition, it can be observed that, for Se@NiFe and FePc/Se@NiFe samples, the representative Raman peaks lied on 125, 197, and 550, 670 cm^{-1} belong to Ni_3Se_4 and $NiFe(OH)_X$. However, FePc/Se@Ni exhibits the Ni_3Se_4 and $Ni(OH)_X$ phase. As reported, the amorphous $NiFe(OH)_X$ and $Ni(OH)_X$ phases are the catalytically active phases in the course of OER[50,51]. The enhancement of activity is contributed to their ability to efficiently accelerate the rate-determining step. Besides, the existence of FePc can obtain both graphitic carbon (G-band) and disorder carbon (D-band) with high electrical conductivity and modified electronic structure in the electrocatalytic process. As observed from Figure 1C and D, the SSA and porous volumes of FePc/Se@NiFe were estimated to be 22.6 $m^2 g^{-1}$ and 0.16 $cm^3 g^{-1}$, as confirmed by the BET method, which is smaller than NiFe-LDH and FePc precursors but larger than other selenides [Supplementary Figure 1C and D]. Due to the large SSA and pore volume of FePc/Se@NiFe, it is beneficial for interfacial electrons and mass transfer, and catalytic activity is improved.

Next, the surface chemical composition of FePc/Se@NiFe and FePc samples, as well as the intrinsic interaction between electronic structure and electrocatalytic performance, were evaluated by XPS tests. As demonstrated in Supplementary Figure 2, in the XPS study spectrum for FePc/Se@NiFe, the co-existence of these signals including C, N, O, Se, Ni, and Fe were found, whereas the Se and Ni signals were absent in FePc. The percentage of surface element atoms is displayed in the insertion table. All data were calibrated with 284.8 eV of C 1s. Compared to FePc, the high-resolution C1s XPS spectral peak of FePc/Se@NiFe [Figure 2A], in order to express strong π-π interactions, moves in the direction of low coupling energy. Typically, the coupling energy reduction exhibits an electronic shielding effect, enhanced by increasing the electron density[52]. As described in Figure 2B, the N 1s XPS spectra of FePc/Se@NiFe were deconvoluted into pyridinic-N/C-N and pyrrolic-N/Fe-N. The abundance of pyridinic-N and Fe-N species in the FePc/Se@NiFe catalyst can serve as real active sites, which are beneficial for ORR electrocatalytic activity[53]. The N 1s peaks of the FePc are at 399.0 and 400.6 eV. Undoubtedly, the N 1s in the FePc/Se@NiFe shifted to the lower coupling energy and the Fe 2p XPS spectra for FePc/Se@NiFe corresponds to the FePc shifted to the higher energy [Figure 2C]. These results indicate that there is an electron donation from the centered Fe ions to the neighboring N atoms, alleviating the significant association with intermediates containing N and O, resulting the approval of the release of N-site O_2[54,55]. Furthermore, the two peaks found at 707.2 and 720.1 eV for FePc/Se@NiFe were ascribed to zero-valence metallic Fe $2p^{3/2}$ and Fe $2p^{1/2}$. The occurrence of Fe^0 may be due to the reduction of iron ions by hydrazine hydrate with strong reducibility during the hydrothermal process. Three peaks, which correspond to the Ni-Se, Ni $2p^{3/2}$, and shakeup satellite peaks, were deconvoluted from the elevated Ni $2p^{3/2}$ XPS spectrum of FePc/Se@NiFe at energies of 853.5, 856.2, and 861.9 eV, respectively [Figure 2D]. The Ni-Se bonding further confirms the existence of Ni_3Se_4 in the FePc/Se@NiFe sample. In Figure 2E, the high-resolution Se 3d spectrum able could be separated into three peaks. The strong peaks at 54.7 eV from Se $3d_{5/2}$ and 55.7 eV from Se $3d_{3/2}$ can be ascribed to Ni-Se banding and zero-valence Se moiety, which agrees well with earlier findings. The strong peaks at 59.3 eV can be ascribed to the SeO_X due to the oxidation of the sample surface. The formation of SeO_X can accelerate the charge transfer as well as the reaction kinetics of the OER reaction process[56]. The deconvoluted O 1s

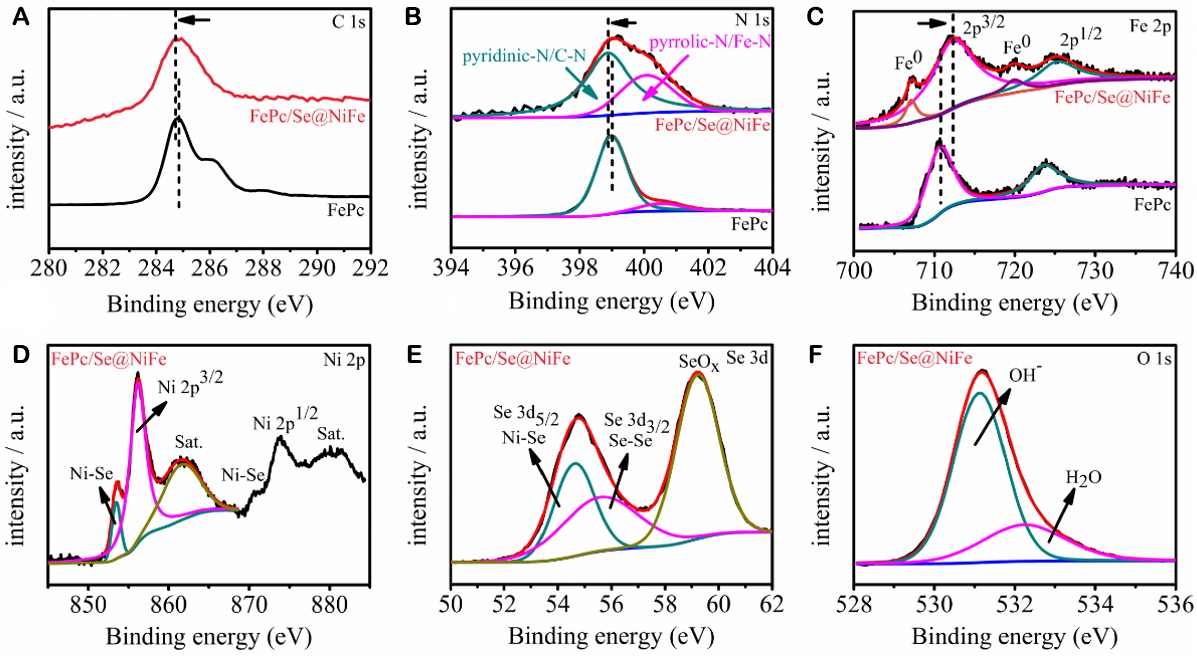

Figure 2. High-resolution XPS spectra of (A) C 1s, (B) N 1s, and (C) Fe 2p in the FePc and FePc/Se@NiFe. High-resolution XPS spectra of (D) Ni 2p, (E) Se 3d, (F) O 1s, and (F) O 1s for FePc/Se@NiFe.

spectrum of FePc/Se@NiFe supports the results inferred from the Raman spectra as the OH^- groups indicate the presence of $NiFe(OH)_X$ [Figure 2F]. In addition, the strong peak of O 1s spectrum at 532.3 eV is corresponding to physically adsorbed H_2O molecular.

The morphology of precursors and FePc/Se@NiFe catalyst were characterized by SEM techniques. As described in Supplementary Figure 3A and B, pure FePc exhibits a highly aggregated granular state with a rough surface, in contrast to the manufactured NiFe-LDH precursors, which are formed of irregular polygonal thin nanosheets with very smooth surfaces. Compared with pure NiFe-LDH and FePc, the FePc/Se@NiFe catalyst exhibited a lot of irregular nanoparticles homogeneously scattered on carbon [Figure 3A]. Similar observations are made on Se@NiFe, FePc/Se@Ni, and FePc/Se@Fe [Supplementary Figure 3C-E]. The shape of the NiFe-LDH nanosheet changed significantly from nanosheets to irregular nanoparticles, indicating that excessive selenization caused damage to the nanosheets structure[57]. In Figure 3B, the TEM image of FePc/Se@NiFe also reveals a mass of nanoparticles in the carbon layer, which is consistent with the SEM findings. HRTEM shows that the tri-phase nanocrystalline coating exhibits an amorphous structure, as marked on the left side of the white lines [Figure 3C]. A crystalline-amorphous interface growth is beneficial for the OER catalysis, which not only facilitates the adsorption of OH* intermediates but also accelerates the formation of OOH*[58]. The lattice spacings of 0.269 and 0.266 nm, which correspond to the (-312) and (-402) crystal planes of Ni_3Se_4, respectively, can be distinctly visualized in Figure 3D. In addition, lattice fringes with spacings of 0.245 nm and 0.469 nm attributed to the (400) plane of Fe_3O_4 and the (11-1) plane of Se are also clearly displayed. This result is the same as the previous XRD. TEM mapping images of FePc/Se@NiFe in Figure 3E-K show the elements of C, N, O, Fe, Ni, and Se are evenly dispersed.

ORR and OER catalytic performance

The Fe-N_4 structure possessed by FePc is considered to be the catalytically active site of ORR. In order to judge the oxygen reduction performance of the prepared catalysts, CV scans were carried out in N_2-saturated and O_2-saturated 0.1M KOH electrolyte solutions, respectively. As presented in

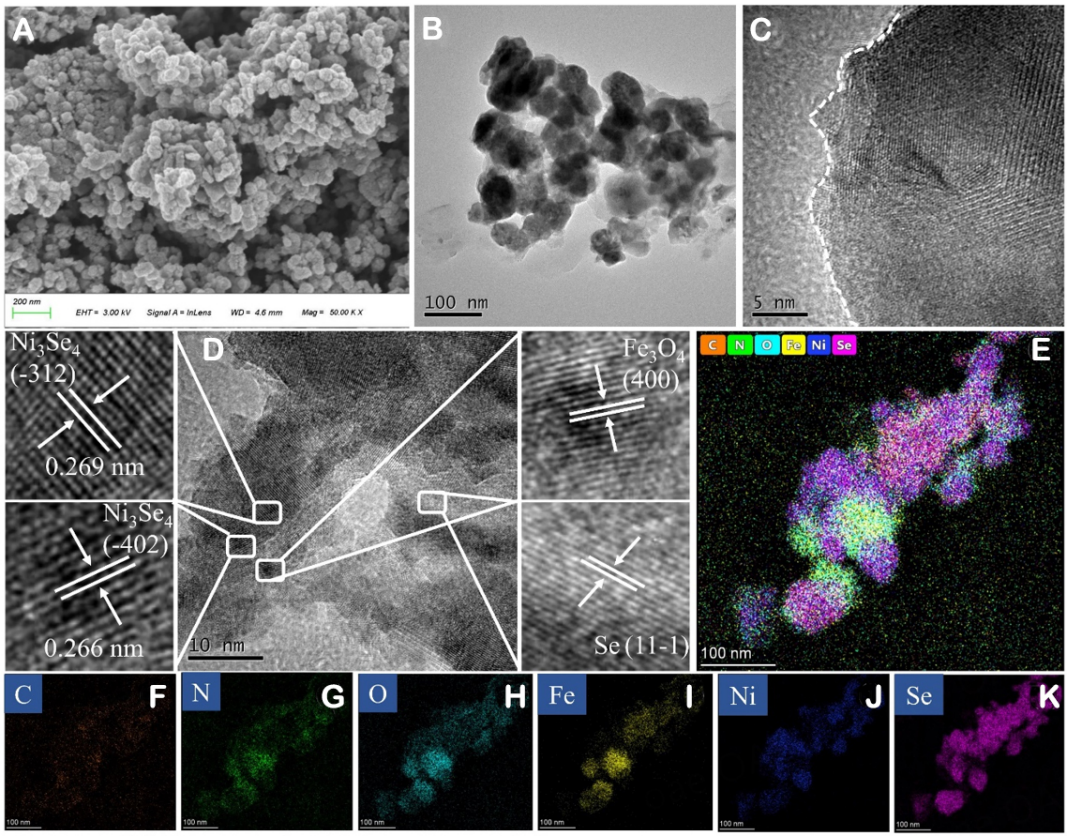

Figure 3. (A) SEM, (B) TEM, (C and D) HRTEM, and (E-K) EDX mapping images of FePc/Se@NiFe electrocatalyst.

Supplementary Figure 4A, all electrode catalysts exhibited significant redox peaks in the O_2-saturated solution, revealing the ORR performance of the prepared catalysts relative to the N_2-saturated electrolyte. The FePc/Se@NiFe displays a cathodic reduction peak at 0.90 V (*vs.* RHE). It is higher than 0.886 V for FePc, 0.60 V for NiFe-LDH, 0.70 V for Se@NiFe, and 0.877 V for Pt/C, indicating its prominent ORR activity. The LSV curves further confirm the superior electroactivity of the FePc/Se@NiFe which the rotating speed is 1,600 rpm [Figure 4A and B]. Specifically, the E_{onset}, $E_{1/2}$ and J_L of FePc/Se@NiFe are 0.977 V, 0.928 V and 4.58 mA/cm^2, respectively. This value is comparable to conventional Pt/C (1.03 V, 0.92 V, and 5.4 mA/cm^2), much more positive than other comparative catalysts [Supplementary Figure 4B and C]. The Tafel slope gets to be used to evaluate the kinetics of electrocatalytic reactions. The Tafel slopes shown in Figure 4C and Supplementary Figure 4D are in the following sequence: FePc/Se@NiFe (31.7 mV/dec) < FePc (43.6 mV/dec) < Pt/C (66.1 mV/dec) < Se@NiFe (100.7 mV/dec) < NiFe-LDH (115.8 mV/dec), revealing better ORR kinetics of the FePc/Se@NiFe. By overcoming the diffusion limitation, FePc/Se@NiFe indicates that the limit current stage increases linearly with increasing speed [Supplementary Figure 4E and F]. The K-L demonstrates that the average n of FePc/Se@NiFe approach to the theoretical value of 4.0, suggesting that the FePc/Se@NiFe possesses a complete reaction pathway for catalytic ORR process. Simultaneously, the RRDE test was further conducted to demonstrate the n and yield of the intermediate H_2O_2. As shown in Figure 4D, the n and H_2O_2 yield of FePc/Se@NiFe are ~3.99 and below 1%, respectively, both of which are better than 3.96 and below 3% of Pt/C. These results are consistent with the above RDE data, and confirm the 4e$^-$ transfer pathway for ORR again. The stability must be considered in practical applications. ADT was tested in 0.1 M KOH electrolyte solution saturated with O_2. Going through 5,000 continuous cycles, the $E_{1/2}$ of FePc/Se@NiFe has almost no shift, while an obvious

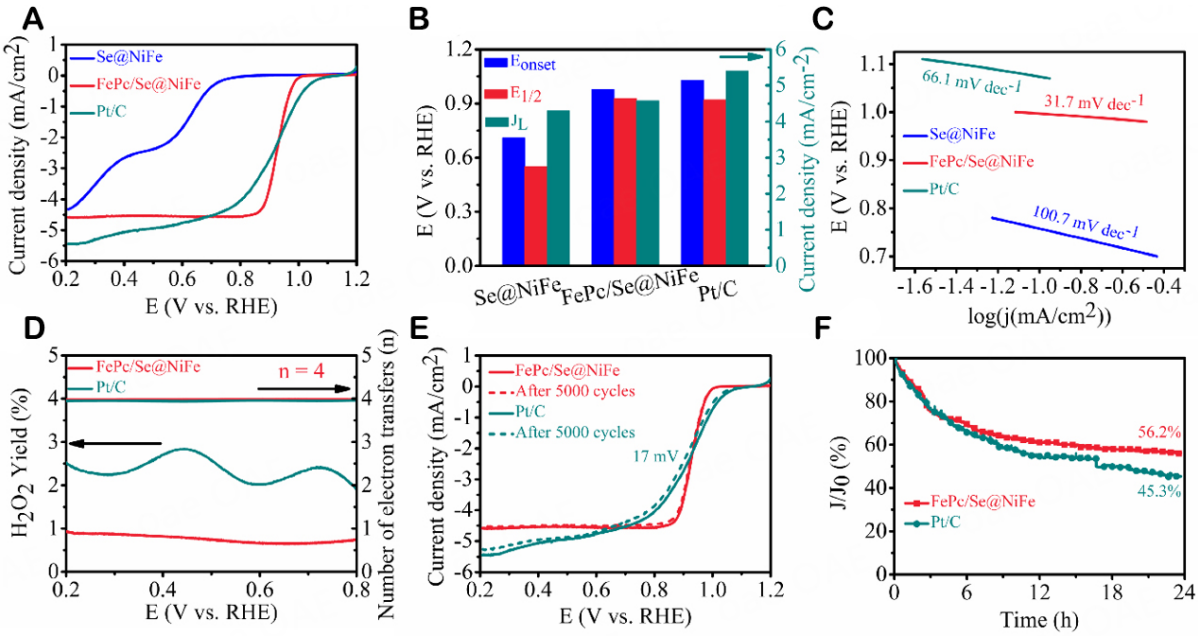

Figure 4. (A) LSV curves, (B) corresponding E_{onset}, $E_{1/2}$ and J_L, and (C) Tafel plots of FePc, FePc/Se@NiFe and 20% Pt/C in O_2-saturated 0.1 M KOH at 1,600 rpm, (D) Calculated n and H_2O_2 yield, (E) LSV recorded before and after ADT for 5,000 cycles, and (F) ORR I-T tests of FePc/Se@NiFe and 20% Pt/C.

$E_{1/2}$ shift (~17 mV) is found in commercial Pt/C [Figure 4E], proving the exceptional stability of FePc/Se@NiFe. The prominent durability of FePc/Se@NiFe was also demonstrated using the I-T test lasting 24 h at 0.6 V (*vs.* RHE). As can be appreciated from Figure 4F, the FePc/Se@NiFe catalyst retains 56.2% of the initial limiting current density, while the standard Pt/C catalyst only retains 45.3% of the initial current. Furthermore, the XRD patterns for FePc/Se@NiFe through 5,000 continuous cycles still showed clear signals of Se, Fe_3O_4, and Ni_3Se_4 crystal phases, demonstrating its outstanding stability. The SEM image displays negligible changes after 5,000 ADT cycles, again implying excellent stability [Supplementary Figure 5A and B]. These results indicate that FePc/Se@NiFe is an excellent catalyst with stability for the ORR. In addition, the C_{dl} is measured to evaluate the ECSA of those electrocatalysts, because ECSA is proportional to the abundant active sites in the catalysts [Supplementary Figure 6A-E]. As displayed in Supplementary Figure 6F, FePc/Se@NiFe (29.7 cm^2) has the greatest ECSA value compared to other catalysts, evidencing more active sites in FePc/Se@NiFe catalyst. From the above electrochemical test results, the superb ORR activity of FePc/Se@NiFe is due to the following two reasons: (1) FePc itself has a special Fe-N_4 active site and a low energy barrier during ORR processes; (2) The efficient Fe-N_4 single atoms site and selenated transition metal hydroxide cooperate to promote ORR activity.

To demonstrate the bifunctional activity, the electrocatalytic OER performance of samples under O_2 saturated 1.0 M KOH electrolyte was estimated using LSV, as illustrated in Figure 5A and B and Supplementary Figure 7A and B. The FePc/Se@NiFe showed a low overpotential of 320 mV at 10 mA cm^2, which is much smaller than Se@NiFe (338 mV), FePc/Se@Ni (360 mV), FePc/Se@Fe (652 mV), FePc (600 mV), NiFe-LDH (390 mV) and RuO_2 (375 mV), demonstrating its superior electrocatalytic activity toward OER. The OER reaction kinetics associated with all samples are evaluated by using the Tafel slopes. As detailed in Figure 5C and Supplementary Figure 7C, the corresponding Tafel slope of FePc/Se@NiFe (55.6 mV dec^{-1}) is significantly smaller than the slopes obtained for Se@NiFe (81.8 mV dec^{-1}), FePc/Se@Ni (134.6 mV dec^{-1}), FePc/Se@Fe (234.5 mV dec^{-1}), FePc (509.6 mV dec^{-1}), NiFe-LDH

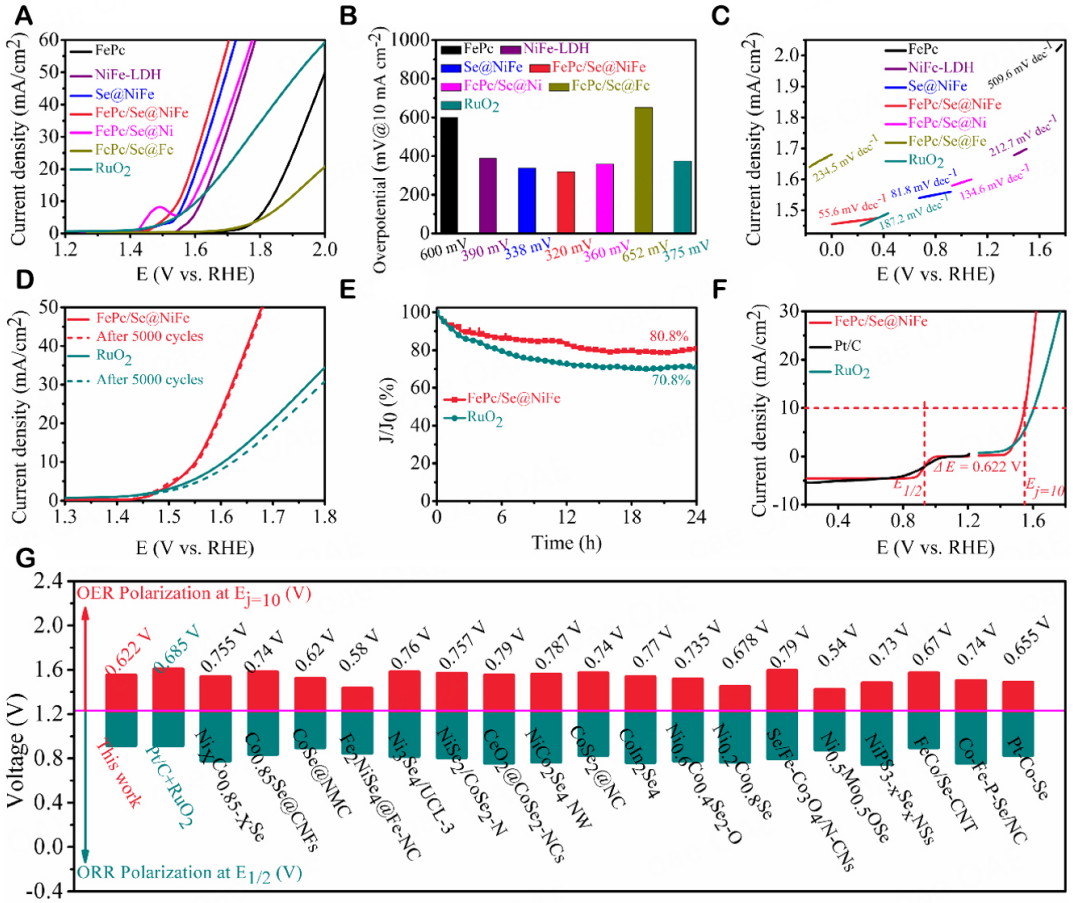

Figure 5. (A) LSV curves, (B) Corresponding overpotentials at 10 mA cm^{-2} (η_{10}), and (C) Tafel plots of Se@NiFe, FePc/Se@NiFe, FePc/Se@Ni, FePc/Se@Fe and RuO_2 in O_2-saturated 1.0 M KOH. (D) LSV recorded before and after ADT for 5,000 cycles and (E) OER I-T tests of FePc/Se@NiFe and RuO_2 at overpotential. (F) Polarization curves of FePc/Se@NiFe for dual-functional catalytic activity. (G) Dual-functional electrocatalytic activity of the FePc/Se@NiFe, Pt/C + RuO_2, and the previously reported electrocatalysts based on transition metal selenides.

(212.7 mV dec^{-1}) and the state-of-the-art RuO_2 catalyst (187.2 mV dec^{-1}). Then, the FePc/Se@NiFe also exhibits excellent durability in terms of OER. As depicted in Figure 5D, the FePc/Se@NiFe display almost a negligible decay of OER activity after 5,000 CV cycles through an ADT. However, the overpotential of RuO_2 increased significantly under the same testing conditions. After the ADT test, there is no noticeable change in the structure and morphology of FePc/Se@NiFe, as evident from the XRD and SEM in Supplementary Figure 5C and D. Furthermore, I-T examinations also are implemented to detect the durability of FePc/Se@NiFe at a given potential of 1.55 V (*vs.* RHE). As displayed in Figure 5E, FePc/Se@NiFe can retain its 80.8% catalytic activity after 24 h stability tests. In contrast, the current response of RuO_2 manifests significant fluctuations with a low retention rate of initial current densities (70.8%), suggesting further the excellent durability of FePc/Se@NiFe. In general, the dual-functional electrocatalytic activity and reversibility are estimated from the potential difference ΔE ($E = E_{j=10} - E_{1/2}$), where a smaller value of E implies better dual-functional activity. Remarkably, the FePc/Se@NiFe electrocatalyst reached an impressive ΔE value of 0.622 V, which is better than FePc (0.91 V), NiFe-LDH (0.96 V), Pt/C + RuO_2 (0.685 V) [Supplementary Figure 7D] and most previously reported high-performance dual-functional catalysts based on transition metal selenides [Figure 5F and G]. The smallest potential gap indicates the tremendous potential of FePc/Se@NiFe for practical application in rechargeable ZABs. Exceptional

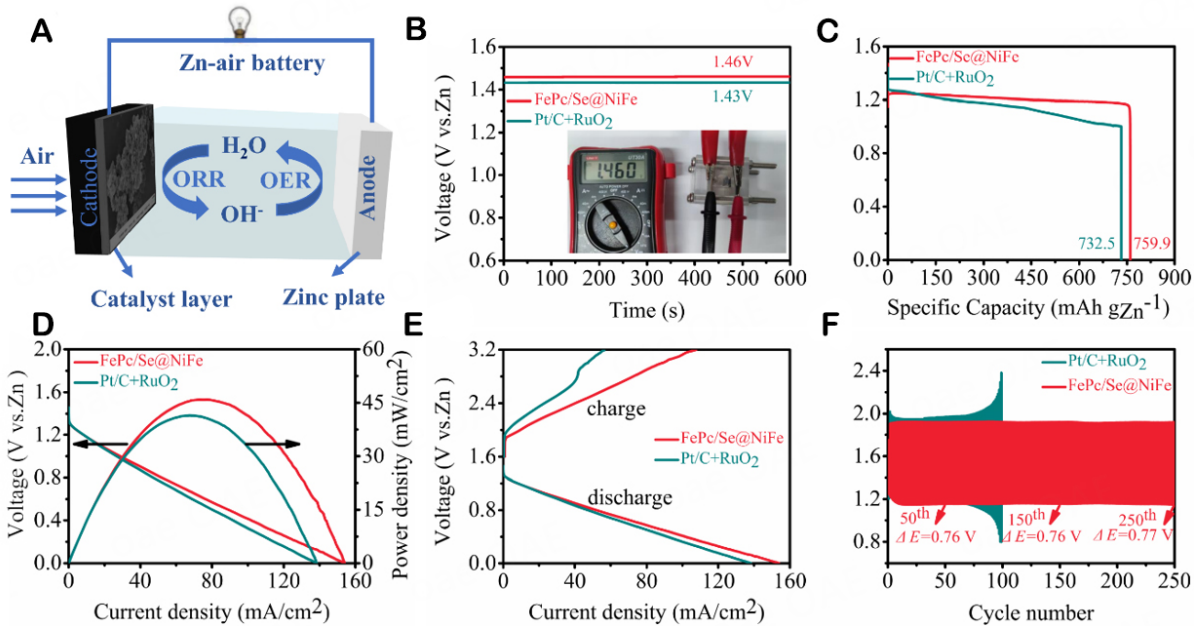

Figure 6. (A) Schematic illustration of a rechargeable ZAB with FePc/Se@NiFe as the air cathode, (B) OCVs plot (inset: the photograph of the OCV), (C) Specific capacity curves, (D) Discharge polarization curves and corresponding power densities, (E) Charge-discharge curves, and (F) Long-term cycling stability of ZAB based on FePc/Se@NiFe and 20% Pt/C + RuO_2.

electrochemical OER performances can be mainly summarized in the following factors. First, the presence of Ni_3Se_4 preferred nanocrystalline active sites can significantly reduce the overpotential of OER process. Second, the incorporation of FePc in FePc/Se@NiFe can make metal active areas more visible, generating graphitization and disordered carbon, as well as ion transport channels, which provide active sites and reaction sites required for OER electrocatalysis, accelerate electron/ion/proton transfer, and reduce the energy barrier of rate-determining reaction intermediates.

Rechargeable ZABs performance

Based on the excellent ORR and OER dual-functional catalytic activity of FePc/Se@NiFe, a rechargeable liquid ZAB was assembled with a Zn sheet anode, an air cathode, and a 6.0 M KOH + 0.2 M NH_4Cl electrolyte, as schematically illustrated in Figure 6A. The FePc/Se@NiFe based battery possesses a high OCV of ~1.46 V [Figure 6B], much higher than Pt/C + IrO_2 battery (~1.43 V), demonstrating the FePc/Se@NiFe displays higher output voltages at practical cell configurations. Also, the specific capacity of the ZAB is assessed by normalizing it to the mass of zinc consumed during the discharging process. The FePc/Se@NiFe based battery achieves a specific capacity of 759.9 mAh g_{Zn}^{-1}, which is ~92.7% of theoretical capacitance (820 mAh g_{Zn}^{-1}, Figure 6C). This value exceeds the 732.5 mAh g_{Zn}^{-1} of Pt/C + RuO_2. Figure 6D shows the discharge polarization curves of the ZABs. The maximum power density of the FePc/Se@NiFe battery is as high as 45.9 mW cm^{-2}, surpassing that of the Pt/C + RuO_2 battery (41.5 mW cm^{-2}). The charge-discharge polarization curve of a typical rechargeable battery shows that the charge-discharge voltage gap of FePc/Se@NiFe cells is narrower in various current densities than that of Pt/C + RuO_2 batteries [Figure 6E]. Galvanostatic charge-discharge cycling tests at a current density of 2 mA cm^{-2} (10 min discharge and 10 min charge) are used to assess the endurance of ZABs based on FePc/Se@NiFe or Pt/C + RuO_2, as illustrated in Figure 6F. On ZABs built with FePc/Se@NiFe, the charge-discharge voltage gap does not appear to alter (250 cycles). Furthermore, the charge-discharge potential difference of FePc/Se@NiFe is increased from the initial 0.76 V to the final 0.77 V. In contrast, rechargeable ZABs containing commercially available Pt/C + RuO_2 cathodes operate after 100 cycles, have a relatively large voltage gap and poor stability, and the

durability of FePc/Se@NiFe-based rechargeable ZABs is obvious. All of these outstanding battery properties prove that three-phase FePc/Se@NiFe is excellent for efficient, durable rechargeable ZABs.

CONCLUSION

In summary, the FePc mixed nickel-iron bimetallic selenide electrocatalysts for high-performance ORR and OER catalysis in basic media have successfully been synthesized by a facile and effective hydrothermal method. FePc was introduced to generate Fe-N_4 structures with graphitized and disordered carbon, Se@NiFe was used to derive the Se, Fe_3O_4 and Ni_3Se_4 crystal phases, Fe-N_4 was formed to impart ORR activity, and Ni_3Se_4 moieties were in charge of OER. The as-prepared FePc/Se@NiFe catalyst manifests superior electrocatalytic activities toward ORR ($E_{1/2}$ ~0.928 V) and OER ($E_{j=10}$ ~320 mV), outperforms that of the conventional Pt/C and RuO_2 catalysts. The ΔE was only 0.622 V, better than that of Pt/C + RuO_2 electrocatalysts (~0.685 V) and most of the previous state-of-the-art dual-functional transition metal selenide catalysts. Moreover, the catalyst possesses a prominent durability for the ORR and OER processes after 5,000 cycles ADT and 24 h I-T. The higher open circuit voltage, power density, specific capacity, lower charge/discharge overpotential, and longer cycle stability endow FePc/Se@NiFe with superior ZAB performance over Pt/C + RuO_2 hybrid catalysts. This work is expected to guide the synthesis of other non-precious metal oxygen bifunctional catalysts from active site design and their successful application in clean energy storage and conversion devices.

DECLARATIONS

Authors' contributions

Conceptualization, Methodology, and Writing the draft of the manuscript: Li G
Contributed to the Methodology of this work: Sheng K
Electrochemical measurements: Lei Y
Provided some help in writing the draft of the manuscript: Zhang F, Yang J
Materials characterization: Chang B
Funding acquisition, review, and editing: Zheng L
Funding acquisition, writing-review, and editing: Wang X

Availability of data and materials

The data supporting this work can be found in the Supplementary Material.

Financial support and sponsorship

This work was supported financially by Key Project of Strategic New Industry of Hunan Province (No. 2019GK2032), National Key Research and Development Program of China (No. 2018YFB0104200), Science and Technology Innovation Program of Hunan Province (No. 2020RC2075), and Hunan Provincial Natural Science Foundation of China (No. 2022JJ30560).

Conflict of interest

All authors declared that there are no conflicts of interest.

Ethical approval and consent to participate

Not applicable.

Consent for publication

Not applicable.

REFERENCES

1. Sekhon SS, Lee J, Park J. Biomass-derived bifunctional electrocatalysts for oxygen reduction and evolution reaction: a review. *J Energy Chem* 2022;65:149-72. DOI
2. Lyu D, Yao S, Ali A, Tian ZQ, Tsiakaras P, Shen PK. N, S codoped carbon matrix-encapsulated Co_9S_8 nanoparticles as a highly efficient and durable bifunctional oxygen redox electrocatalyst for rechargeable Zn-air batteries. *Adv Energy Mater* 2021;11:2101249. DOI
3. Zhang H, Zhao M, Liu H, et al. Ultrastable FeCo bifunctional electrocatalyst on Se-doped CNTs for liquid and flexible all-solid-state rechargeable Zn-air batteries. *Nano Lett* 2021;21:2255-64. DOI
4. Yang H, Gao S, Rao D, Yan X. Designing superior bifunctional electrocatalyst with high-purity pyrrole-type CoN_4 and adjacent metallic cobalt sites for rechargeable Zn-air batteries. *Energy Stor Mater* 2022;46:553-62. DOI
5. Wang X, Raghupathy RKM, Querebillo CJ, et al. Interfacial covalent bonds regulated electron-deficient 2D black phosphorus for electrocatalytic oxygen reactions. *Adv Mater* 2021;33:e2008752. DOI
6. Ramakrishnan S, Velusamy DB, Sengodan S, et al. Rational design of multifunctional electrocatalyst: an approach towards efficient overall water splitting and rechargeable flexible solid-state zinc-air battery. *Appl Catal B Environ* 2022;300:120752. DOI
7. Arafat Y, Azhar MR, Zhong Y, Abid HR, Tadé MO, Shao Z. Advances in zeolite imidazolate frameworks (ZIFs) derived bifunctional oxygen electrocatalysts and their application in zinc-air batteries. *Adv Energy Mater* 2021;11:2100514. DOI
8. Zhao CX, Liu JN, Wang J, Ren D, Li BQ, Zhang Q. Recent advances of noble-metal-free bifunctional oxygen reduction and evolution electrocatalysts. *Chem Soc Rev* 2021;50:7745-78. DOI
9. Zhu Y, Song L, Song N, Li M, Wang C, Lu X. Bifunctional and efficient CoS_2-C@MoS_2 core-shell nanofiber electrocatalyst for water splitting. *ACS Sustain Chem Eng* 2019;7:2899-905. DOI
10. Logeshwaran N, Ramakrishnan S, Chandrasekaran SS, et al. An efficient and durable trifunctional electrocatalyst for zinc-air batteries driven overall water splitting. *Appl Catal B Environ* 2021;297:120405. DOI
11. Wang S, Zhang L, Li X, et al. Sponge-like nickel phosphide-carbon nanotube hybrid electrodes for efficient hydrogen evolution over a wide pH range. *Nano Res* 2017;10:415-25. DOI
12. Ge Y, Dong P, Craig SR, Ajayan PM, Ye M, Shen J. Transforming nickel hydroxide into 3D prussian blue analogue array to obtain Ni_2P/Fe_2P for efficient hydrogen evolution reaction. *Adv Energy Mater* 2018;8:1800484. DOI
13. Xu S, Wang M, Saranya G, et al. Pressure-driven catalyst synthesis of Co-doped Fe_3C@Carbon nano-onions for efficient oxygen evolution reaction. *Appl Catal B Environ* 2020;268:118385. DOI
14. Li M, Zhu Y, Wang H, Wang C, Pinna N, Lu X. Ni strongly coupled with Mo_2C encapsulated in nitrogen-doped carbon nanofibers as robust bifunctional catalyst for overall water splitting. *Adv Energy Mater* 2019;9:1803185. DOI
15. Lv Y, Batool A, Wei Y, et al. Homogeneously distributed NiFe alloy nanoparticles on 3D carbon fiber network as a bifunctional electrocatalyst for overall water splitting. *ChemElectroChem* 2019;6:2497-502. DOI
16. Dionigi F, Zhu J, Zeng Z, et al. Intrinsic electrocatalytic activity for oxygen evolution of crystalline 3D-transition metal layered double hydroxides. *Angew Chem Int Ed* 2021;60:14446-57. DOI PubMed PMC
17. Wang Z, Liu W, Hu Y, et al. Cr-doped CoFe layered double hydroxides: highly efficient and robust bifunctional electrocatalyst for the oxidation of water and urea. *Appl Catal B Environ* 2020;272:118959. DOI
18. Liu S, Jiang Y, Yang M, et al. Highly conductive and metallic cobalt-nickel selenide nanorods supported on Ni foam as an efficient electrocatalyst for alkaline water splitting. *Nanoscale* 2019;11:7959-66. DOI
19. Kumar RS, Prabhakaran S, Ramakrishnan S, et al. Developing outstanding bifunctional electrocatalysts for rechargeable Zn-air batteries using high-purity spinel-type $ZnCo_2Se_4$ nanoparticles. *Small* 2023:e2207096. DOI
20. Lai C, Gong M, Zhou Y, et al. Sulphur modulated Ni_3FeN supported on N/S co-doped graphene boosts rechargeable/flexible Zn-air battery performance. *Appl Catal B Environ* 2020;274:119086. DOI
21. Shi G, Yu C, Fan Z, Li J, Yuan M. Graphdiyne-supported NiFe layered double hydroxide nanosheets as functional electrocatalysts for oxygen evolution. *ACS Appl Mater Interfaces* 2019;11:2662-9. DOI
22. Yin P, Wu G, Wang X, et al. NiCo-LDH nanosheets strongly coupled with GO-CNTs as a hybrid electrocatalyst for oxygen evolution reaction. *Nano Res* 2021;14:4783-8. DOI
23. Sun H, Yang J, Li J, et al. Synergistic coupling of NiTe nanoarrays with RuO_2 and NiFe-LDH layers for high-efficiency electrochemical-/photovoltage-driven overall water splitting. *Appl Catal B Environ* 2020;272:118988. DOI
24. Lin J, Wang P, Wang H, et al. Defect-rich heterogeneous MoS_2/NiS_2 nanosheets electrocatalysts for efficient overall water splitting. *Adv Sci* 2019;6:1900246. DOI PubMed PMC
25. Chen F, Ji S, Liu Q, et al. Rational design of hierarchically core-shell structured Ni_3S_2@$NiMoO_4$ nanowires for electrochemical energy storage. *Small* 2018;14:e1800791. DOI
26. Liu H, Ma X, Rao Y, et al. Heteromorphic $NiCo_2S_4$/Ni_3S_2/Ni foam as a self-standing electrode for hydrogen evolution reaction in alkaline solution. *ACS Appl Mater Interfaces* 2018;10:10890-7. DOI
27. Li Q, Wang X, Tang K, Wang M, Wang C, Yan C. Electronic modulation of electrocatalytically active center of Cu_7S_4 nanodisks by

cobalt-doping for highly efficient oxygen evolution reaction. *ACS Nano* 2017;11:12230-9. DOI

28. Li Y, Zhang H, Jiang M, Zhang Q, He P, Sun X. 3D self-supported Fe-doped Ni_2P nanosheet arrays as bifunctional catalysts for overall water splitting. *Adv Funct Mater* 2017;27:1702513. DOI
29. Ju M, Wang X, Long X, Yang S. Recent advances in transition metal based compound catalysts for water splitting from the perspective of crystal engineering. *CrystEngComm* 2020;22:1531-40. DOI
30. Yan Y, Wang P, Lin J, Cao J, Qi J. Modification strategies on transition metal-based electrocatalysts for efficient water splitting. *J Energy Chem* 2021;58:446-62. DOI
31. Xu W, Zhu S, Liang Y, Cui Z, Yang X, Inoue A. A nanoporous metal phosphide catalyst for bifunctional water splitting. *J Mater Chem A* 2018;6:5574-9. DOI
32. Yu L, Zhou H, Sun J, et al. Cu nanowires shelled with NiFe layered double hydroxide nanosheets as bifunctional electrocatalysts for overall water splitting. *Energy Environ Sci* 2017;10:1820-7. DOI
33. Hong Y, Kim KM, Ryu JH, et al. Dual-phase engineering of nickel boride-hydroxide nanoparticles toward high-performance water oxidation electrocatalysts. *Adv Funct Mater* 2020;30:2004330. DOI
34. Huang K, Sun Y, Zhang Y, Wang X, Zhang W, Feng S. Hollow-structured metal oxides as oxygen-related catalysts. *Adv Mater* 2019;31:e1801430. DOI
35. Wang R, Liu B, You S, et al. Three-dimensional Ni_3Se_4 flowers integrated with ultrathin carbon layer with strong electronic interactions for boosting oxygen reduction/evolution reactions. *Chem Eng J* 2022;430:132720. DOI
36. Zheng X, Han X, Liu H, et al. Controllable synthesis of Ni_xSe ($0.5 \leq x \leq 1$) Nanocrystals for efficient rechargeable zinc-air batteries and water splitting. *ACS Appl Mater Interfaces* 2018;10:13675-84. DOI
37. Douka AI, Xu Y, Yang H, et al. A zeolitic-imidazole frameworks-derived interconnected macroporous carbon matrix for efficient oxygen electrocatalysis in rechargeable zinc-air batteries. *Adv Mater* 2020;32:e2002170. DOI
38. Zhao C, Liu J, Li B, et al. Multiscale construction of bifunctional electrocatalysts for long-lifespan rechargeable zinc-air batteries. *Adv Funct Mater* 2020;30:2003619. DOI
39. Chen D, Zhu J, Mu X, et al. Nitrogen-doped carbon coupled $FeNi_3$ intermetallic compound as advanced bifunctional electrocatalyst for OER, ORR and zn-air batteries. *Appl Catal B Environ* 2020;268:118729. DOI
40. Zhang M, Zhang J, Ran S, et al. A robust bifunctional catalyst for rechargeable Zn-air batteries: ultrathin NiFe-LDH nanowalls vertically anchored on soybean-derived Fe-N-C matrix. *Nano Res* 2021;14:1175-86. DOI
41. Jiao L, Wan G, Zhang R, Zhou H, Yu SH, Jiang HL. From metal-organic frameworks to single-atom Fe implanted N-doped porous carbons: efficient oxygen reduction in both alkaline and acidic media. *Angew Chem Int Ed* 2018;57:8525-9. DOI
42. Yu X, Lai S, Xin S, et al. Coupling of iron phthalocyanine at carbon defect site via π-π stacking for enhanced oxygen reduction reaction. *Appl Catal B Environ* 2021;280:119437. DOI
43. Li G, Sheng K, Lei Y, et al. Facile synthesis of Fe_3C-dominated $Fe/Fe_3C/FeN_{0.0324}$ multiphase nanocrystals embedded in nitrogen-modified graphitized carbon as efficient pH-universal catalyst for oxygen reduction reaction and zinc-air battery. *Chem Eng J* 2023;451:138823. DOI
44. Li Y, Wang Z, Ali Z, et al. Monodisperse Fe_3O_4 spheres: large-scale controlled synthesis in the absence of surfactants and chemical kinetic process. *Sci China Mater* 2019;62:1488-95. DOI
45. Zhang J, Tian X, He T, et al. In situ formation of Ni_3Se_4 nanorod arrays as versatile electrocatalysts for electrochemical oxidation reactions in hybrid water electrolysis. *J Mater Chem A* 2018;6:15653-8. DOI
46. Li Z, Wang X, Li X, Zhang W. Reduced graphene oxide (rGO) coated porous nanosphere TiO_2@Se composite as cathode material for high-performance reversible Al-Se batteries. *Chem Eng J* 2020;400:126000. DOI
47. Yan L, Xu Z, Liu X, et al. Integrating trifunctional Co@NC-CNTs@NiFe-LDH electrocatalysts with arrays of porous triangle carbon plates for high-power-density rechargeable Zn-air batteries and self-powered water splitting. *Chem Eng J* 2022;446:137049. DOI
48. Gultom NS, Abdullah H, Hsu C, Kuo D. Activating nickel iron layer double hydroxide for alkaline hydrogen evolution reaction and overall water splitting by electrodepositing nickel hydroxide. *Chem Eng J* 2021;419:129608. DOI
49. Meng H, Liu X, Chen X, et al. Hybridization of iron phthalocyanine and MoS_2 for high-efficiency and durable oxygen reduction reaction. *J Energy Chem* 2022;71:528-38. DOI
50. Yuan J, Cheng X, Wang H, et al. A superaerophobic bimetallic selenides heterostructure for efficient industrial-level oxygen evolution at ultra-high current densities. *Nanomicro Lett* 2020;12:104. DOI PubMed PMC
51. Liu C, Han Y, Yao L, et al. Engineering bimetallic NiFe-based hydroxides/selenides heterostructure nanosheet arrays for highly-efficient oxygen evolution reaction. *Small* 2021;17:e2007334. DOI
52. Mei Z, Cai S, Zhao G, et al. Boosting the ORR active and Zn-air battery performance through ameliorating the coordination environment of iron phthalocyanine. *Chem Eng J* 2022;430:132691. DOI
53. Chen D, Chen X, Cui Z, et al. Dual-active-site hierarchical architecture containing NiFe-LDH and ZIF-derived carbon-based framework composite as efficient bifunctional oxygen electrocatalysts for durable rechargeable Zn-air batteries. *Chem Eng J* 2020;399:125718. DOI
54. Yang J, Tao J, Isomura T, Yanagi H, Moriguchi I, Nakashima N. A comparative study of iron phthalocyanine electrocatalysts supported on different nanocarbons for oxygen reduction reaction. *Carbon* 2019;145:565-71. DOI
55. Yin Z, Liu X, Cui M, et al. Template synthesis of molybdenum-doped NiFe-layered double hydroxide nanotube as high efficiency electrocatalyst for oxygen evolution reaction. *Mater Today Sustain* 2022;17:100101. DOI

56. Ding K, Hu J, Luo J, et al. Confined N-$CoSe_2$ active sites boost bifunctional oxygen electrocatalysis for rechargeable Zn-air batteries. *Nano Energy* 2022;91:106675. DOI
57. Li Y, Wang X, Sun M, Zhao Z, Wang Z, Qiu J. NiCo(oxy)selenide electrocatalysts *via* anionic regulation for high-performance lithium-sulfur batteries. *J Mater Chem A* 2022;10:5410-9. DOI
58. Yang Y, Wei S, Li Y, Guo D, Liu H, Liu L. Effect of cobalt doping-regulated crystallinity in nickel-iron layered double hydroxide catalyzing oxygen evolution. *Appl Catal B Environ* 2022;314:121491. DOI